Article:

Direct bandgap Group IV epitaxy on Si for laser applications

N. von den Driesch[1*], D. Stange[1], S. Wirths[1], G. Mussler[1], B. Holländer[1], Z. Ikonic[2], J.M. Hartmann[3], T. Stoica[1†], S. Mantl[1], D. Grützmacher[1] and D. Buca[1*]

[1] Peter Grünberg Institute 9 (PGI-9) and JARA-Fundamentals of Future Information Technologies (JARA-FIT), Forschungszentrum Juelich, 52425 Juelich, Germany.

[2] Institute of Microwaves and Photonics, School of Electronic and Electrical Engineering, University of Leeds, Leeds LS2 9JT, United Kingdom.

[3] CEA, LETI, MINATEC Campus, F-38054 Grenoble, France and Univ. Grenoble Alpes, F-38000 Grenoble, France.

*Corresponding Authors: <u>n.von.den.driesch@fz-juelich.de</u> ; <u>d.m.buca@fz-juelich.de</u>

Abstract

The recent observation of a fundamental direct bandgap for GeSn group IV alloys and the demonstration of low temperature lasing provide new perspectives to the fabrication of Si photonic circuits. This work addresses the progress in GeSn alloy epitaxy aiming at room temperature GeSn lasing. Chemical vapor deposition of direct bandgap GeSn alloys with a high Γ- to L-valley energy separation and large thicknesses for efficient optical mode confinement is presented and discussed. Up to 1 µm thick GeSn layers with Sn contents up to 14 at.% were grown on thick relaxed Ge buffers, using Ge_2H_6 and $SnCl_4$ precursors. Strong strain relaxation (up to 81 %) at 12.5 at.% Sn concentration, translating into an increased separation between Γ- and L-valleys of about 60 meV, have been obtained without crystalline structure degradation, as revealed by Rutherford backscattering/ion channeling spectroscopy and Transmission Electron Microscopy. Room temperature transmission/reflection and photoluminescence measurements were performed to probe the optical properties of these alloys. The emission/absorption limit of GeSn alloys can be extended up to 3.5 µm (0.35 eV), making those alloys ideal candidates for optoelectronics in the mid-infrared region. Theoretical net gain calculations indicate that large room temperature laser gains should be reachable even without additional doping.

1. Introduction

Silicon and Germanium, the most commonly used group IV semiconductors, are indirect bandgap semiconductors with the conduction band minimum at the X- or L-points, respectively, and not at the center of the Brillouin zone, as is the valence band maximum. Electron-hole pair recombination hence usually requires phonons in order to preserve momentum. As a consequence of this second order recombination process, the radiative recombination probability is significantly lower than in direct recombination processes, occurring in direct bandgap semiconductors like III-V alloys. This is the main obstacle to the fabrication of efficient group IV light emitters, especially lasers. Despite this fundamental limitation, progress has recently been made concerning the luminescence efficiency of

strain-engineered Ge by inducing high biaxial [1–3] or uniaxial [4,5] tensile strain. Tensile distortion of the Ge lattice modifies the electronic band structure of Ge by reducing the energy difference between the Γ- and L-valleys. Therefore, a large electron population in the Γ-valley becomes available for efficient direct recombination. An alternative approach is the heavy n-type doping of Ge in order to fill up the electronic states in the L-valley up to the Γ-valley [6].

The successful realization of a fundamental direct bandgap group IV semiconductor was achieved by alloying Ge with Sn. The substitutional incorporation of Sn atoms into the cubic Ge lattice has a similar effect as tensile strain in Ge: it reduces the energy separation between the Γ- and L-valley, eventually swapping their positions. For cubic GeSn crystals this transition to a fundamental direct semiconductor occurs at a Sn concentration of approx. 9 at.% [7].

The epitaxial growth of GeSn binaries on Si or Ge results naturally in a large compressive strain, which increases the Γ-L energy separation. It may even lead to an indirect behavior in a compressively strained alloy, which would otherwise be direct if fully strain relaxed. In order to compensate for the effect of compressive strain, larger Sn contents are required. Values up to 17 at.% for GeSn alloys grown pseudomorphically on Ge substrates have previously been shown [8]. A practical approach towards fundamental direct bandgap GeSn at experimentally achievable Sn contents is the realization of strain relaxed alloys. However, for active laser materials both, a high degree of strain relaxation in thick layers together with a low defect density is of paramount importance.

The synthesis of fully strain relaxed GeSn epilayers with device grade quality is a demanding task, mainly due to the metastable nature of this alloy. The low solid solubility of Sn in Ge of approximately 1 at.% [9] and the large lattice mismatch of 15% between α-Sn and the Ge substrate are major hurdles that have to be overcome. Thermal annealing - the most common technique for plastic strain relaxation - is not applicable for Sn-based systems, as severe Sn diffusion leads to poor layer quality [10]. The most efficient way, in our opinion, to fabricate high quality, partially strain relaxed epilayers is to grow several hundred nanometer thick GeSn layers on Ge virtual substrates (Ge-VS). Significant progress has

been made in recent years in epitaxy of these alloys by Chemical Vapor Deposition (CVD) [11–13] and Molecular Beam Epitaxy [14,15]. However, the low growth temperatures required for Sn incorporation still lead to an epitaxial breakdown in thick layers due to a strong increase of surface roughness for Sn concentrations > 10 at.% [14]. Very recently, the ability to grow ~500 nm thick GeSn layers with Sn concentrations of approx. 12.5 at.% Sn has enabled the demonstration of fundamental direct bandgap of these alloys and even lasing[7]. This breakthrough has brought about a new class of materials in group IV, which can revolutionize the Si photonics [16].

In this work we present details on the epitaxial CVD growth and in-depth structural and optical characterization of direct bandgap GeSn alloys aiming for laser fabrication. Most emphasis is placed on binaries with thicknesses up to 1 µm for a complete optical mode confinement and Sn concentrations between 8 and 14 at.% which offer sufficient Γ-L energy difference for efficient laser emission. Atomic Force Microscopy (AFM) for surface morphology, Rutherford backscattering spectroscopy/ion channeling (RBS/C) and cross-sectional Transmission Electron Microscopy (TEM) for crystallinity together with X-Ray Diffraction (XRD) for plastic strain relaxation were used in order to gain insights into the growth mechanism and the relaxation process of those thick GeSn layers. The optical properties were assessed using room-temperature transmission/reflection and photoluminescence measurements. The increase of the Sn content to 14 at.% leads to a reduction of the fundamentally direct bandgap below 0.4 eV extending the window for optical applications above 3 µm. Furthermore, net gain calculations show that the GeSn layers are suitable for room-temperature laser emission in heterostructures, without the necessity of additional doping, as suggested for the tensily strained Ge approach [6].

2. Experimental Part

The growth of the GeSn layers was performed on cyclically annealed, 2.5 – 2.7 µm thick Ge virtual substrates (Ge-VS) on Si(100) [17]. A 200 mm AIXTRON TRICENT® reduced-pressure CVD

reactor with a showerhead design that yields a uniform distribution of the precursor gases over the whole wafer surface, was used for synthesis of GeSn binaries. Commercially available precursors such as digermane (Ge_2H_6) and tintetrachloride ($SnCl_4$) were employed. The weaker Ge-Ge bond strength (about 2.9 eV) in Ge_2H_6 molecules compared to Ge-H bonds in GeH_4 (about 3.6 eV) [18], which is typically used for SiGe and Ge epitaxy, facilitates the chemical decomposition of the former at low growth temperatures. It thus ensures high growth rates at low temperatures, which is a favorable critical precondition for the incorporation of high amounts of Sn atoms into the Ge matrix. Furthermore, it helps suppressing Sn surface segregation and bulk precipitation, usually the cause for crystalline quality degradation of the GeSn alloys. While Ge_2H_6 is gaseous, $SnCl_4$ is a liquid precursor. A bubbler system is therefore used to vaporize the precursor, while the amount of $SnCl_4$ radicals delivered into the reactor is controlled by the bubbler temperature and the H_2 carrier gas flow. Prior to growth, an ex-situ HF vapor etching of native oxide is performed in an automated single wafer cleaning tool, followed by an in-situ pre-epi bake at about 850°C in order to finish removing contaminants and start from pristine Ge surfaces. After reactor cooling to the desired growth temperature, the precursor gases along with nitrogen, used as carrier gas, were introduced into the chamber at a total gas flow of a few slm. The GeSn alloys addressed here were grown at a fixed precursor partial pressure ratio p_{Ge2H6} / p_{SnCl4} = 220, while the precise control of the Sn content in the GeSn binaries was achieved mainly by adjusting the growth temperature.

3. Results and Discussion

(a) Growth mechanism/Film growth

The stoichiometry, thickness and crystalline quality of the grown layers were extracted using RBS/C. Measurements were carried out on a Tandetron accelerator with 1.4 MeV He$^+$ ions at a scattering angle of 170°. Fitting the random spectra with the RUMP® simulation software yielded layer

stoichiometry information within an error of less than ±0.5%, while the epitaxial quality and substitutionality of Sn was evaluated via channeling spectra.
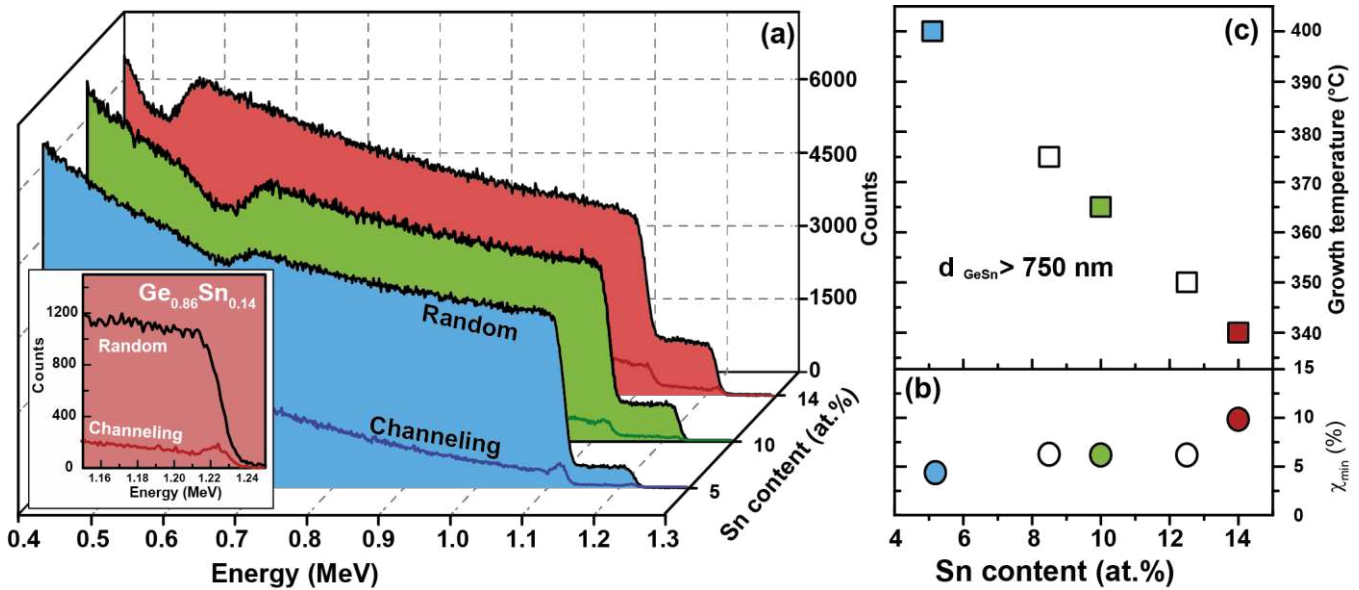

Figure 1. (a) RBS random and channeling spectra for thick GeSn layers with Sn concentrations of 5%, 10% and 14%. Inset: Detail of random and channeling Sn signal for a 1 µm thick $Ge_{0.86}Sn_{0.14}$ sample. (b) *Min. channeling yield* χ_{min} of thick GeSn alloys with different Sn contents. (c) Incorporated Sn content in GeSn alloys as a function of growth temperature.

Figure 1(a) shows the RBS random and channeling spectra of three GeSn layers, with thicknesses of 770 nm, 840 nm and 1.03 µm for Sn concentrations of 5 at.%, 10 at.% and 14 at.%, respectively. The spectra regions between 1.14 MeV and 1.23 MeV comes solely from the Sn atoms in the GeSn layers. The plateaus observed in this region show uniform depth distribution of Sn and allow a clear distinction between layers with different Sn contents. At energies below 1.14 MeV signals of Ge and Sn atoms overlap. The decrease of the RBS signal at energies between 0.4 MeV and 0.6 MeV is associated with the interface between the GeSn alloys and the Ge-VS. In the inset in Figure 1(a) an enlargement of the Sn part of the spectrum from the $Ge_{0.86}Sn_{0.14}$ sample is shown.

The minimum channeling yield χ_{min}, defined by the ratio between channeling and random spectra directly behind the surface peak, is about 5 % - 7 % for Sn contents up to 12.5 at.%, as shown in Figure

6

1(b). A slight increase of χ_{min} to about 9 % is only observed for the 1.03 µm thick $Ge_{0.86}Sn_{0.14}$ sample. The low χ_{min} values indicate not only that the GeSn layers are of high crystalline quality, but also that the Sn atoms occupy almost exclusively substitutional lattice sites. It should be noted that all χ_{min} data points are associated with GeSn layers with thicknesses between 770 nm and 1 µm, and, as we will discuss in the following, with a high degree of strain relaxation.

The degree of alloying is precisely controlled by the process temperature, which is shown in Figure 1(c). At otherwise constant growth parameters like reactor pressure and precursor flows, the Sn concentration in the binary is strongly increased by decreasing the growth temperature. Since the bond strength of Sn-Cl amounts to a value (3.3 eV [19]) even slightly larger than for the Ge-Ge bond in the digermane, differences in thermal decomposition should not have a major influence. Temperature variation also strongly impacts the growth rate. Fig. 2(a) shows the relation between Sn content, and the mean growth rates (defined as the ratio between the GeSn layer thickness determined by RBS and growth time) at different processing temperatures. In a linear segregation model [20], a high growth rate minimizes the interlayer mass transport, reducing the position exchange mechanism between the built-in Sn atoms and arriving Ge surface adatoms, as known from surface mediated epitaxy growth [21]. Therefore, higher growth rates at constant temperature should be linked to higher Sn concentrations in the alloy. In Fig 2(a), the mean growth rate decreases from roughly 35 nm/min down to about 10 nm/min as a result of the growth temperature reduction from 400°C down to 340°C; while the Sn content increases by a factor of about 3, from 5 at.% up to 14 at.%. Thus the temperature-growth rate interplay governs the epitaxial growth: the lower the temperature the higher the Sn content will be. This may be explained by the temperature dependent decrease of the segregation length [20]. The smaller segregation length limits exchanges between subsurface Sn atoms and surface Ge atoms leading to an increase of the Sn content in the alloy. However, to fully suppress kinetically roughening and Sn segregation, which may lead to an epitaxial breakdown, a certain growth rate has to be provided.
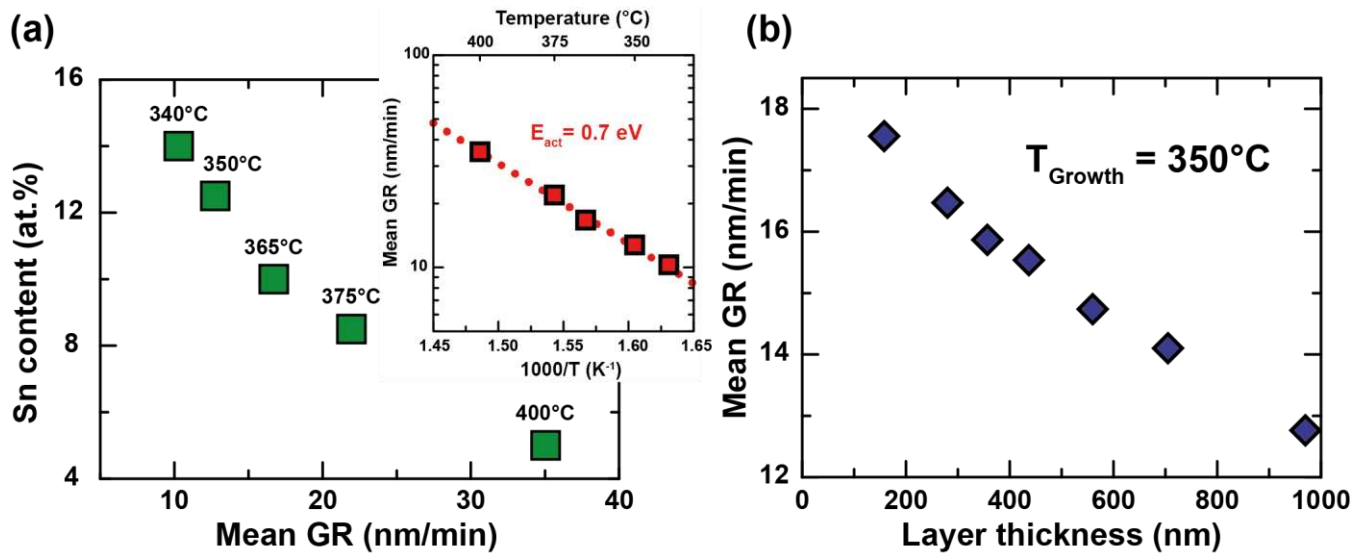
Figure 2. (a): The relation between the Sn content in GeSn binary alloys as a function of mean growth rate and temperature.(inset): Arrhenius plot of the GeSn growth rate as a function of the reverse absolute temperature and the extracted activation energy. (b) GeSn mean growth rate at 350°C as a function of layer thickness (and thus growth duration).

To prove the kinetically limited growth mode, an Arrhenius-plot of the GeSn growth rate as a function of the reverse absolute temperature is provided in the inset of Fig. 2(a). The growth rate increases exponentially with the temperature, as expected when growth is kinetically limited. The here extracted activation energy of about 0.7 eV is slightly higher than the value of 0.6 eV reported in Ref. [22]. The difference may arise from the investigated sample thicknesses: below 100 nm in Ref. [22] and above 750 nm in this work. The impact of the layer thickness on the growth rate of $Ge_{0.875}Sn_{0.125}$ alloys at growth temperature of 350°C is shown in Fig. 2(b). A gradual reduction of the mean growth rate as the GeSn layer thickness increases is observed, decreasing from 17.6 nm/min for a 158 nm thick layer to 12.8 nm/min for a 970 nm thick layer. This thickness dependent growth rate, observed also in other CVD reactor type [11], may be linked to an increase in surface roughness, as discussed in the following section.

(b) Surface morphology

Atomic Force Microscopy (AFM) was used to investigate the evolution of the surface morphology and its root-mean-square (rms) roughness with the GeSn layer thickness. AFM images for various $Ge_{0.875}Sn_{0.125}$ thicknesses are shown in Fig. 3(b)-(f). Layer thickness and the rms value associated to the 10x10 μm^2 scans are provided as insert in each picture. The Ge-VS (Fig. 3(a)) and the pseudomorphic GeSn layer (Fig. 3(b)) are smooth, with the presence of a small amplitude cross-hatch (i.e. undulations with a 1 to 2 µm spatial wavelength, typically), the fingerprint of the regular array of misfit dislocations at the Ge-VS/Si(100) interface [17]. A regular and higher amplitude surface crosshatch along the perpendicular <110> directions is observed for a GeSn layer thickness of 158 nm, related to the periodic strain fields induced by the presence of misfit dislocations at the GeSn/Ge-VS interface resulting in surface energy variation.[23]. The spatial wavelength of the undulations, their amplitude and thus the surface rms roughness increase with the GeSn film thickness. For example the spatial periodicity of the undulations associated with a 970 nm thick layer, (cf. surface shown in Figure 3(f)), which is typically in the 1 µm - 1.5 µm range, is several times that of thinner samples (for instance about 500 nm undulation period in Fig. 3(d)). This is explained by the increasing distance between the dislocated interface and the free surface, resulting in more homogeneous strain field distribution. The formation of mounds is then energetically less favorable; downhill mass transport thus leads to merging of surface undulations. This coalescence of mounds may also explain the reduction in growth rate, shown in Fig. 2(b). Macroscopically, this leads to an increase of the rms roughness values, as seen in Figs. 3(e) and (f).
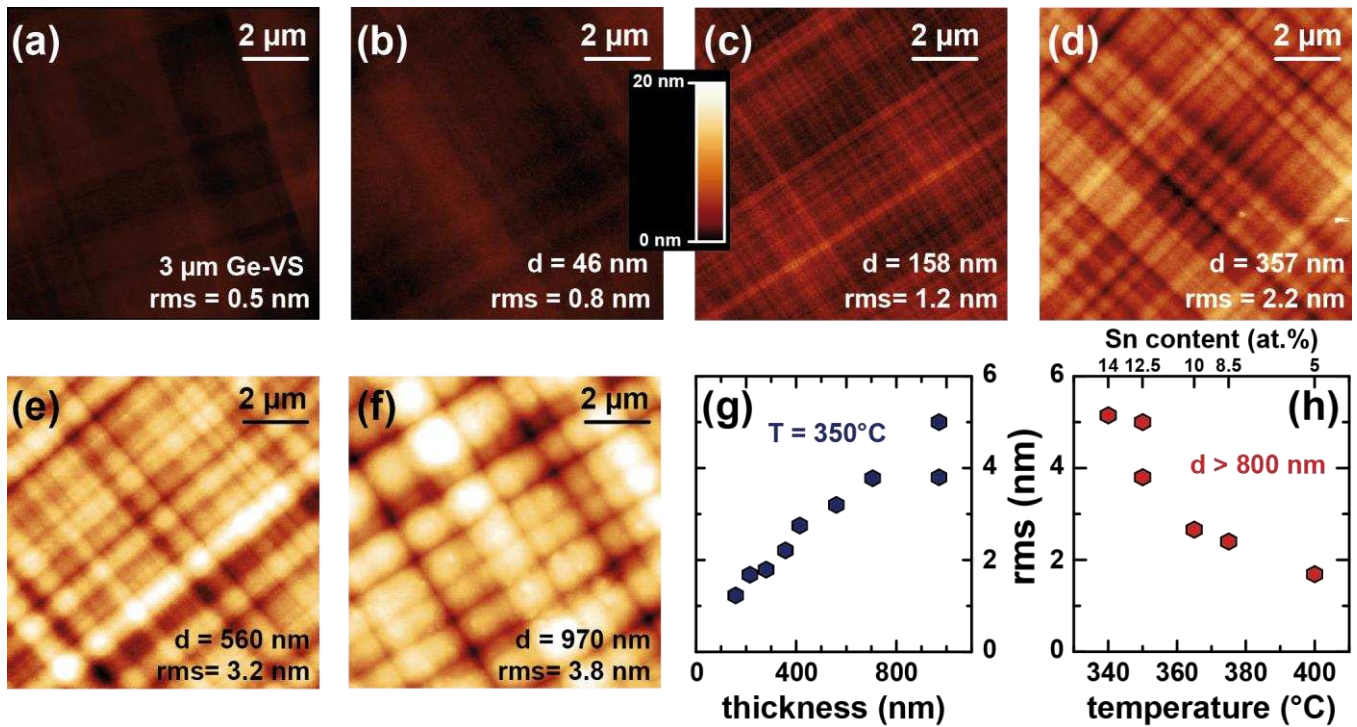
Figure 3. (a)-(f) AFM images of the surface of differently thick $Ge_{0.875}Sn_{0.125}$ layers. Surface rms roughness dependence on the (g) layer thickness and (h) growth temperature for thick layers (800 nm - 1 µm).

The rms roughness, extracted from AFM images, increases almost linearly with the layer thickness, reaching 4 to 5 nm for a 970 nm thick $Ge_{0.875}Sn_{0.125}$ sample (see Fig. 3(g)). Local variations exist on a given wafer despite the lack of major segregations, explaining the two data points for the thickest sample. Such an rms thickness dependence is known from low temperature growth e.g. of Ge layers on Si(100) substrates [24] and is linked to a kinetically limited adatom mobility. The rms roughness value itself is comparable to state-of-the-art values for a few micrometer thick SiGe buffers at the technological interesting Ge content of about 30 % [25]. Finally, Fig. 3(h) illustrates the strong surface roughness decrease as the growth temperature increases. Only GeSn layers with thickness between 800 nm to 1000 nm are compared. This behavior can be explained by the enhanced surface diffusion/mobility of adatoms. Higher temperature helps to overcome the energy barriers for adatom diffusion. Of course this only holds true as long as surface segregation is still suppressed. In addition,

10

the decreased Sn incorporation in the alloy for elevated growth temperatures (see Fig. 1(b)) reduces the strain field at the interface and subsequently the surface undulation.

It should be noted that we have not observed any Sn segregations or crystalline to amorphous transitions in any of the investigated samples, regardless of growth temperature and thickness, in contrast to previous reports in the literature [11].

(c) Strain relaxation in GeSn alloys

Layers grown above the critical thickness plastically relax to larger in-plane lattice constants. The elastic strain in the layers, or equivalently, the degree of strain relaxation compared to pseudomorphic growth on Ge-VS, is independently determined by measuring the in-plane and out-of-plane lattice constants by X-Ray Diffraction Reciprocal Space Mapping (XRD - RSM) and by ion channeling angular yield RBS scans.

RSM around the asymmetric (224) reflection were performed using a Bruker D8 high-resolution diffractometer and the K_α wavelength of Cu (1.54 A). The RSM for the 970 nm thick $Ge_{0.875}Sn_{0.125}$ sample is shown in Figure 4(a). Three peaks are identified, which are associated with the Si(001) substrate, the Ge-VS and the GeSn layer on top. Due to the smaller lattice constant of the Ge-VS, the epitaxially grown GeSn layers is compressively strained leading to a tetragonal distortion of the crystal lattice. A larger out-of-plane lattice constant, compared to the in-plane one, shifts the RSM GeSn peak above the cubic line in Fig 4(a). Despite its thickness, the layer does not reach full relaxation (cubic structure) indicated by the dotted line. It should be mentioned that the Ge-VS itself is under slight tensile stress ($\varepsilon \sim 0.16\%$), which originates from differences in thermal expansion coefficients between Ge and Si, stressing the buffer after growth [17]. The strain relaxation evolution with the GeSn layer thickness is shown in Figure 4(b), which consists in overlapping RSMs for three different thicknesses. A 46 nm thick GeSn layer with 12 % Sn grown on Ge-VS is fully compressively strained. Indeed, its in-plane lattice constant matches exactly the one from the virtual substrate, indicated by the dotted vertical line. Plastic relaxation of the GeSn alloy can be observed in the second, 172 nm thick GeSn layer, with a

degree of relaxation of about 39%. The thickest (970 nm) GeSn layer shows an even higher degree of relaxation, of about 80%; it is close to the line of full relaxation linking the Ge VS peak to the origin of the reciprocal space. Figure 4(c) summarizes the degree of relaxation (top) and residual strain (bottom) of $Ge_{0.875}Sn_{0.125}$ as a function of layer thickness.
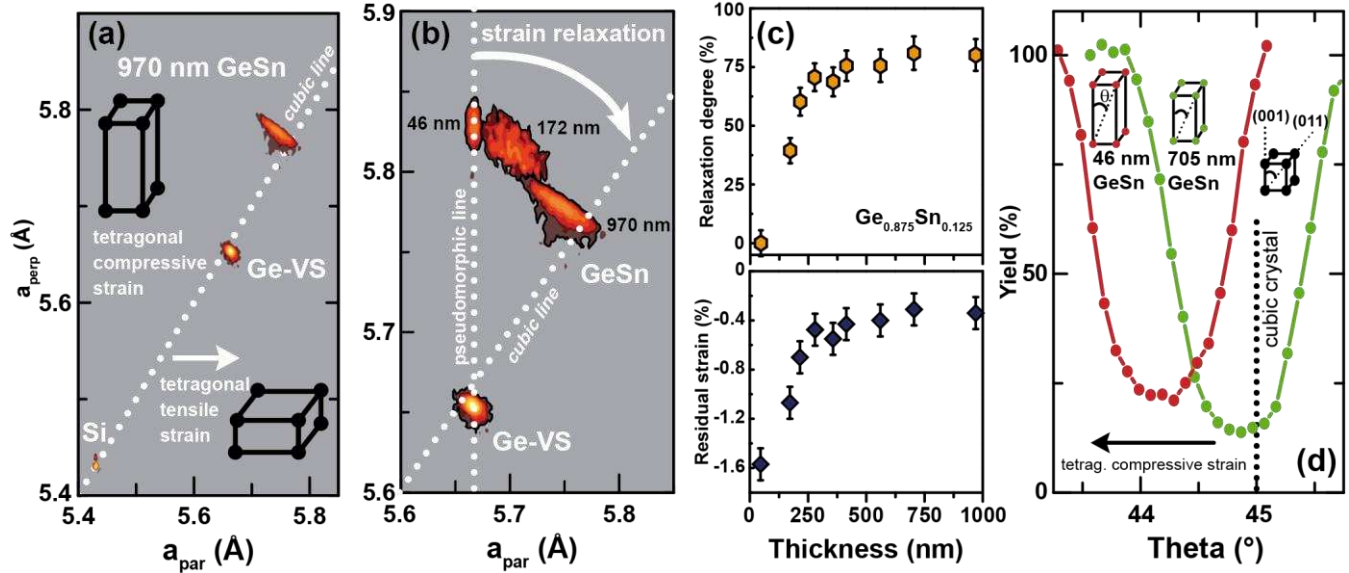

Figure 4. X-Ray Diffraction Reciprocal Space Maps associated with (a) a 970 nm $Ge_{0.875}Sn_{0.125}$ layer and (b) various thickness $Ge_{0.875}Sn_{0.125}$ layers. (c) Strain relaxation (top) and residual compressive strain (bottom) versus GeSn layer thickness. (d) RBS channeling measurements along (011) for 46 nm thick, fully pseudomorphic and 705 nm thick, partially relaxed $Ge_{0.875}Sn_{0.125}$ layers.

Strain is an important parameter for band structure calculations, as it has a critical influence on the directness of the GeSn alloy. For this reason, we have used another strain determination technique, namely ion channeling angular yield scans [26]. Angular scans through the [001] sample normal and the [011] direction along the (100) plane were performed on some of the GeSn layers. Figure 4(d) shows the ion channeling angular yield scan of the Sn backscattering signal for 46 nm and 705 nm thick GeSn layers with 12 and 12.5 at.% Sn, respectively. The position of the minimum yield represents the absolute angle $\theta_{[011]}$ between the [001] sample normal and the inclined [011] direction. For cubic lattices such as

12

bulk, unstrained Si or fully relaxed GeSn, the angle between [001] and [011] has a value of 45°. Compressive tetragonal strain, present in GeSn layers grown on Ge-VS or Si substrates, leads to smaller angles $\theta = (45° - |\Delta\theta_{[011]}|)$. The sign of the shift is negative for compressively strained layers and positive for tensile strained crystals. For symmetric (isotropic) biaxial relaxation, the amount of tetragonal strain is related to the angular shift as

$$\varepsilon_T = -2 \cdot \Delta\theta_{[011]}.$$

The measured angular shift of $\Delta\theta_{[011]} = -0.82°$ corresponds here to a tetragonal strain of -2.9 % in the 46 nm GeSn layer as theoretically expected for full pseudomorphic growth on a Ge-VS. Meanwhile, the angular shift of $\Delta\theta_{[011]} = -0.15°$ for the 705 nm $Ge_{0.875}Sn_{0.125}$ sample corresponds to a residual tetragonal strain of about -0.5 %. From elastic theory one can calculate the in-plane biaxial strain from tetragonal strain values, yielding -1.6 % (46 nm layer) and -0.3 % (705 nm layer). These values are in agreement with strain values coming from XRD-RSM (cf. Fig 4(c)).

The origin of strain relaxation and the overall morphology of the binary alloys were then investigated by cross-sectional transmission electron microscopy (TEM), using a Tecnai G2 TF20 S-TWIN system operating at 200 kV. The understanding of the creation of defects is of utmost importance. They indeed act as centers for non-radiative carrier recombination and can therefore strongly decrease the light emission efficiency of our GeSn layers, which would be detrimental for lasing.
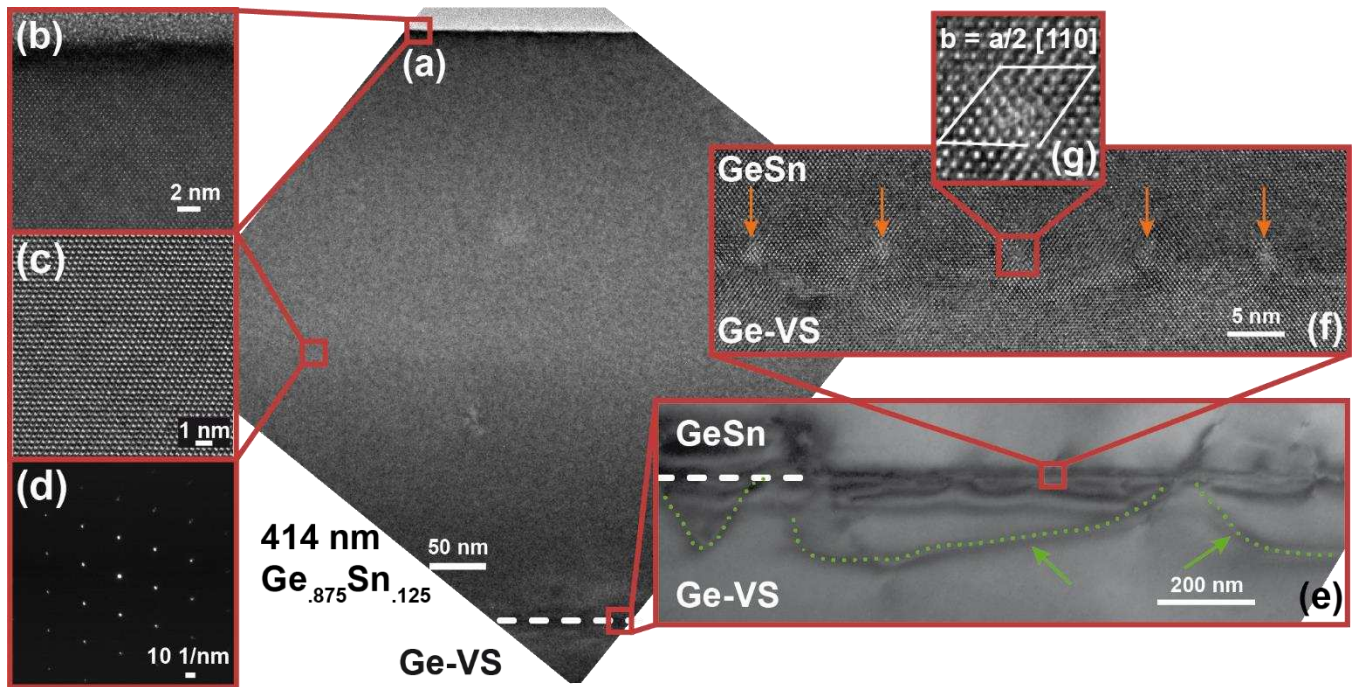
Figure 5. XTEM micrographs of a GeSn layer: (a) overview, (b) surface, (c) and (d) crystallinity and diffraction pattern from the layer volume, (e) interface between GeSn and the Ge-VS, (f) defects near the interface, (g) the Burgers vector associated with a Lomer dislocation.

The cross-sectional TEM (XTEM) image of a 414 nm thick GeSn layer is shown in Fig. 5(a), with a zoom on the surface in (b). The high-resolution XTEM image (c) and the selective area diffraction pattern (d) from the center of the layer show the high crystalline quality. Despite the strong plastic relaxation of that layer (R = 76%), nearly no 60° dislocations were found, yielding an upper threading dislocation density (TDD) limit of 5×10^6 cm^{-2}. All defects appear to be confined near the interface between the GeSn layer and the Ge-VS, where the misfit strain is relaxed via a dense misfit dislocation (MD) network, as shown in Fig. 5(e) and (f). The average spacing between the dislocations is determined to about 12.5 nm. High-resolution XTEM analyses taken at about 3° off the (110) pole around the (220) vector enabled us to identify some of them as pure edge dislocations (Figure 5(g)). These so-called Lomer dislocations have a Burgers vector parallel to the interface and are, therefore, the most efficient strain releasing type of dislocations.

14

In addition to the aforementioned defects at the interface, dislocation loops in the Ge layer pinned at the GeSn/Ge interface were found. They are indicated by green arrows and dotted lines in Fig 5(e). We assume that a large number of point defects introduced during growth and required for compensating the large compressive misfit strain at the interface, typical for low temperature epitaxy [20], are at the origin of these dislocation half-loops. The loops enlargement by acquiring point defects is accompanied by the extension of the misfit segments formed at the interface. It results in the formation of a strain-relaxing network of misfit dislocations at the GeSn/Ge interface. A similar relaxation process has been observed in Si/SiGe heterostructures when a low temperature buffer was used as a point defects source, before the growth of a graded, strain relaxing SiGe layer [27].

Such a strain relaxation process, with defects confined at the interface to the Ge-VS underneath, yields high-quality optical properties in optoelectronics devices. Indeed, the presence of "bulk" defects is a major cause of light emitting devices' degradation. In the following we will investigate the optical properties of our alloys, and the potential of strain-relaxed thick layers for optoelectronic applications. Previously, optical data were restricted to indirect GeSn alloys [12,15,28], i.e. with a low Sn content and/or large residual compressive strain. Here, we study only fundamental direct bandgap GeSn alloys or alloys at the indirect-to-direct transition, i.e. thick layers with high Sn concentrations.

(d) Optical characterization.

Transmission/reflection (T/R) and photoluminescence (PL) spectroscopy were used to study the optical properties of laser active media GeSn alloys, aiming for room temperature lasing. Room temperature T/R and PL measurements were performed using a Bruker VERTEX 80V FTIR spectrometer system. The detector used for T/R spectra collection was a liquid nitrogen cooled HgCdTe detector; both a halogen and SiC lamp were used for obtaining incident light in Near- and Mid-Infrared, respectively. The T/R spectra were acquired using an integrating sphere with reflecting sample holder, both coated with Au. PL measurements were performed using a cw frequency doubled Nd:YAG laser with an excitation wavelength of 532 nm as a light excitation source. A nitrogen-cooled InSb detector

was employed for spectra collection. A cut-off filter at about 3 µm ensured a minimized contribution of thermal radiation to PL spectra.

The reflection spectra along with PL room temperature spectra for three different thickness $Ge_{0.875}Sn_{0.125}$ layers are displayed in Figure 6(a)-(c). PL peaks are at the same energy as the onset of strong absorption regions in the reflection spectra, evidencing band-to-band recombination in direct bandgap alloys. The intensity of the room temperature PL emission definitely increases when the residual compressive strain decreases, i.e. when the GeSn layer thickness increases. This is fully in line with an increased directness of the GeSn semiconductor, as discussed in more details later on (larger carrier density occupying the Γ-valley). The monotonic decrease of the PL peak energy when the built-in compressive strain in $Ge_{0.875}Sn_{0.125}$ alloys decreases is shown in Fig. 6(d). Such a trend is in agreement with a strain-induced change in the bandgap energy. The inset shows that the strongest PL peak position change is observed for layer thicknesses of about 400 nm. In thicker GeSn epilayers, the PL peak position only weakly decreases. This behavior resembles Fig. 4(c) strain relaxation behavior, proving that plastic strain relaxation is most likely the source of this PL peak energy shift.
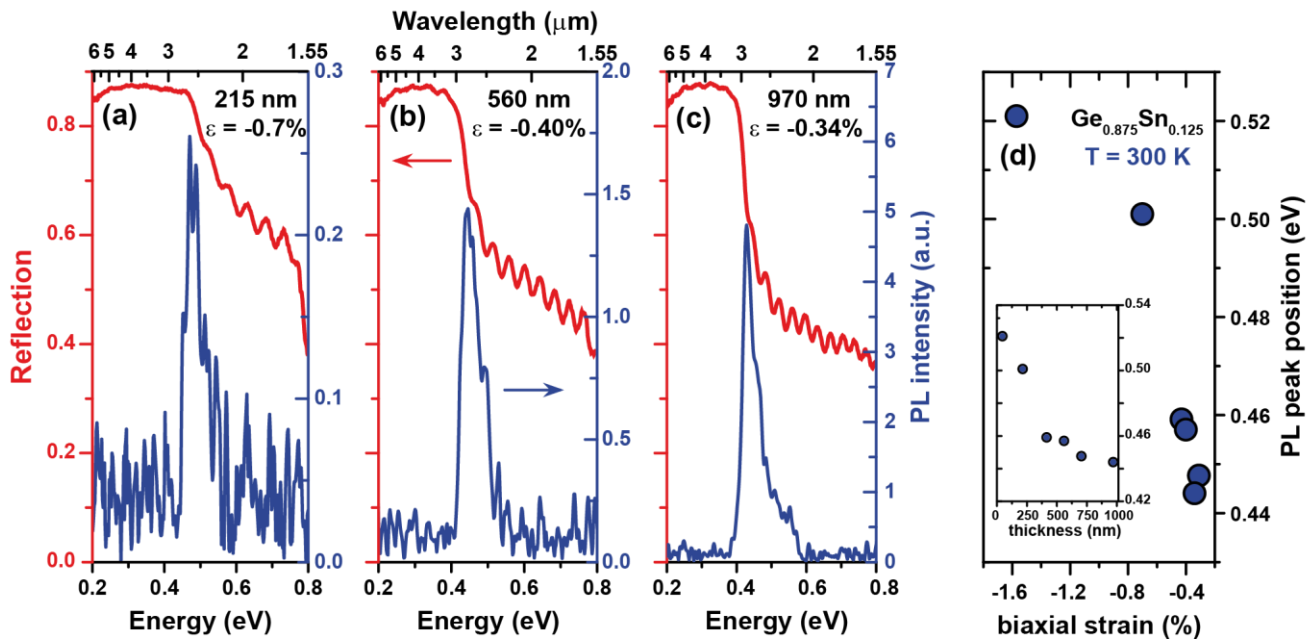
Figure 6. Room temperature reflection and PL spectra associated with $Ge_{0.875}Sn_{0.125}$ layers that are either (a) 215 nm *(ε=-0.70%)*, *(b) 560 nm (ε=-0.40%)* or (c) 970 nm *(ε=-0.34%)* thick. (d) Strain and thickness (inset) dependence of the PL peak position.

Electronic band structure calculations, the details of which are described in the supplement of Ref. 7 [7], are shown in Fig. 7 for $Ge_{0.875}Sn_{0.125}$ alloys with different residual compressive strain values. The degree of relaxation in these layers is shown on the upper scale. The rather thin GeSn alloys grown pseudomorphically (R = 0 %) on Ge-VS show a fundamentally indirect bandgap. Decreasing the residual compressive strain to about -1.05 % leads to an indirect-to-direct transition of the bandgap and any further strain reduction leads to an increase of the directness ΔE, defined as the difference between the direct Γ- and the indirect L-valley reaching about 80 meV for a fully relaxed $Ge_{0.875}Sn_{0.125}$ layer, as shown in Fig. 7(b).

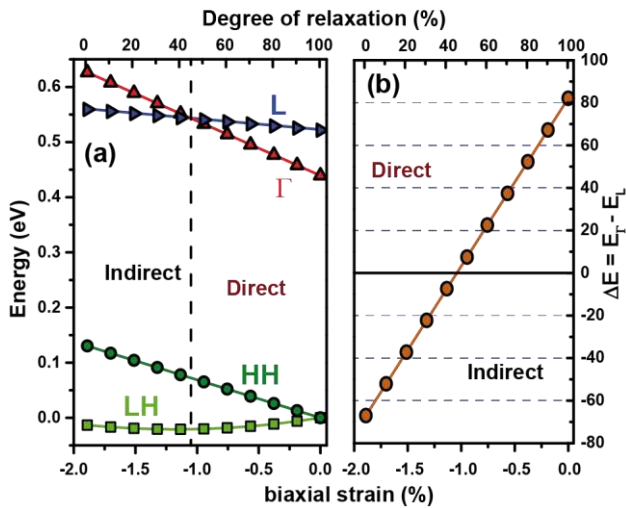**Figure 7**. Electronic b*and structure calculation and directness, ΔE* = E_Γ-E_L for $Ge_{0.875}Sn_{0.125}$ layers as a function of compressive strain (lower scale) and degree of strain relaxation (upper scale).

Optically pumped lasing has already been demonstrated at temperatures up to 90 K in $Ge_{0.875}Sn_{0.125}$ layers [7]. If a direct bandgap is a necessary requirement for lasing, a larger directness, i.e. through increase of a Sn content or strain relaxation, is expected to increase the light emission efficiency. This is illustrated by PL spectra shown in Fig. 6(a), (b) and (c). The 215 nm thick GeSn layer (-0.70 % strain) from Fig. 6(a) should indeed have a fundamental direct bandgap according to calculations. The PL intensity definitely increases for an even thicker layer with the same Sn content, as shown in Fig. 6(b) and (c). This effect is likely due to the increased influence of the strain-relaxed material in thicker layers which, via its improved degree of directness (and hence an enhanced direct recombination), reduces the influence of non-radiative recombination paths. Since the L-valley has a much higher effective mass and, therefore, density of states compared to the Γ-valley, even a small increase in directness can strongly increase the number of electrons available for spontaneous radiative emission. The suppression of Γ- to L-valley carrier transfer is indeed of primary importance in order to improve the laser performance. A degree of strain relaxation as high as possible is therefore necessary for lasing devices and other optoelectronics purposes.

Another way to reach a larger ΔE is to increase the Sn content in the GeSn alloy. However, incorporating higher amounts of Sn atoms in GeSn alloys will shift the bandgap to lower energies, pushing the light emission towards 3 µm. This is illustrated in Figure 8(a) by integrating sphere reflectance spectra for thick GeSn layers with Sn contents between 8.5 and 14 at.%. The Ge-VS spectrum is also provided for comparison. Increased absorption with a threshold energy at 0.35 eV (3.5 µm) for the 14 at.% Sn sample allows the use of the material as Short- to Mid-wavelength infrared photodetectors. The corresponding Sn-dependent room temperature PL spectra for these GeSn samples are shown in Fig 8(b). The higher spontaneous radiative recombination rates of direct energy transitions lead to a remarkable PL emission increase in the thick 12.5 at.% Sn sample compared to the 10 at.% one. Electronic band structure calculations showed that the $Ge_{0.875}Sn_{0.125}$ and $Ge_{0.86}Sn_{0.14}$ alloys are deeper in the fundamental direct bandgap region while the $Ge_{0.915}Sn_{0.085}$ and $Ge_{0.9}Sn_{0.1}$ layers are just at

the indirect-to-direct bandgap transition. The 1 μm thick $Ge_{0.86}Sn_{0.14}$ sample has a peak position of about 0.39 eV, which corresponds to a photon wavelength of nearly 3.2 μm. This value proves the suitability of our GeSn layers as mid-IR light emitters.
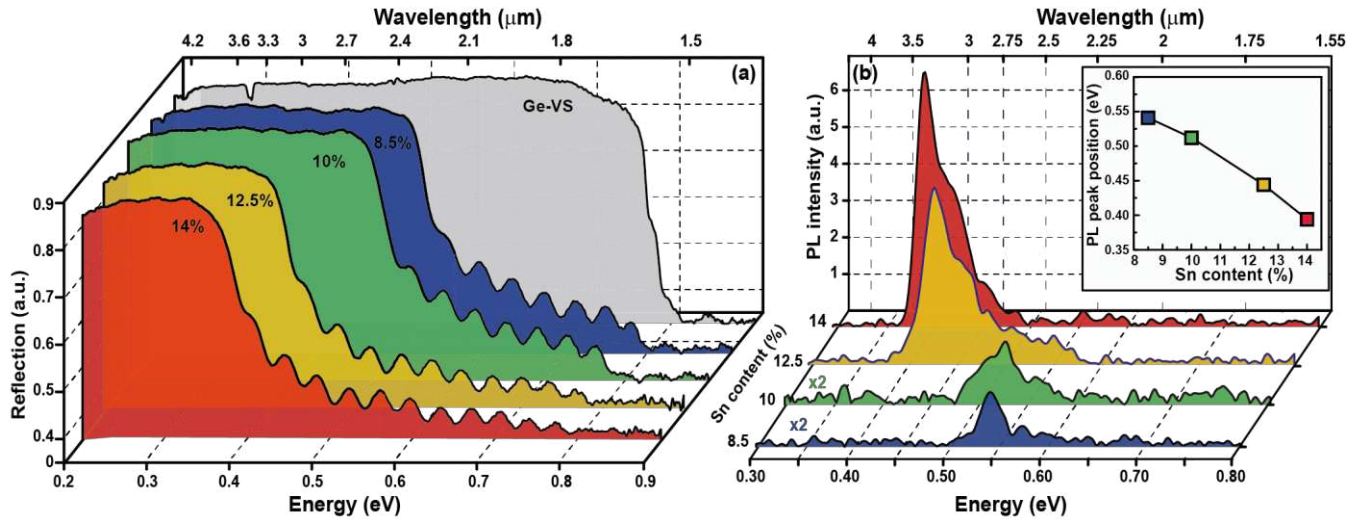

Figure 8. Room temperature reflection (a) and PL spectra (b) for thick GeSn layers (800-1000 nm) with Sn contents between 8.5 and 14 at.%. The Ge-VS spectrum is provided as reference. Inset of (b): Room temperature PL peak positions.

(e) Optical gain calculation

Optical gain calculations have been performed for the thick 12.5 at.% and 14 at.% Sn samples (compressively strained at -0.3% and -0.6%, respectively). We indeed want to investigate their electrically pumped lasing potential. Calculations were performed using 8-band **k.p** model that takes into account the influence of strain [29,30]. This model includes interband transitions from valence to conduction band, which may lead to absorption or gain, and also the inter-valence band transitions (between heavy hole (HH), light hole (LH) and spin-orbit (SO) bands), which bring in absorption, as previously described in [13]. These new calculations also account for free carrier absorption (FCA), which limits the net gain, especially at high injected carrier densities and doping concentrations. The conduction band FCA was calculated via the second-order perturbation theory and accounts for acoustic

19

phonons and (for the L-valley only) the optical deformation potential intravalley electron scattering, intervalley scattering, and ionized impurity scattering, as described in [31]. GeSn alloy disorder scattering was also factored in. Finally, the indirect interband transitions, which may bring in (relatively small) absorption or gain [32,33], are also included. The valence band FCA was taken into account in a simplified manner. Comparisons with experimental measurements of absorption coming from holes in Ge [34] indeed indicate that a simple Drude model, e.g. [35], overestimates this absorption. We have therefore adopted the simple fitting expression for Ge [34], deducted thereby the calculated inter-valence band absorption in Ge, and the difference – attributed to come from the scattering-induced part of the absorption by holes – was then used to calculate holes FCA in GeSn alloys, assuming that this part does not depend too strongly on the alloy composition or strain. Ge and Sn material parameters were mostly taken from [36]. A Vegard's Law (with bowing if available) was used in order to determine the properties of GeSn alloys from those of elemental Ge or Sn. Such an approach is not applicable for the Luttinger parameters, however, since their values are positive in Ge and negative in Sn. Therefore, they were calculated using a quadratic fit of [37] data. The intervalley spacing (hence, the electron distribution and thus the gain) definitely depends on the bandgap bowing, which was taken from [38].

Figure 9(a) and (b) show the peak gain values for in-plane polarized light (TE mode) for thick 12.5 at.% and 14 at.% Sn layers. The net gain has been calculated for n-type doping concentrations up to $5 \times 10^{19} \text{cm}^{-3}$ and carrier injection densities between $1 \times 10^{17} \text{ cm}^{-3}$ and $2 \times 10^{19} \text{ cm}^{-3}$.
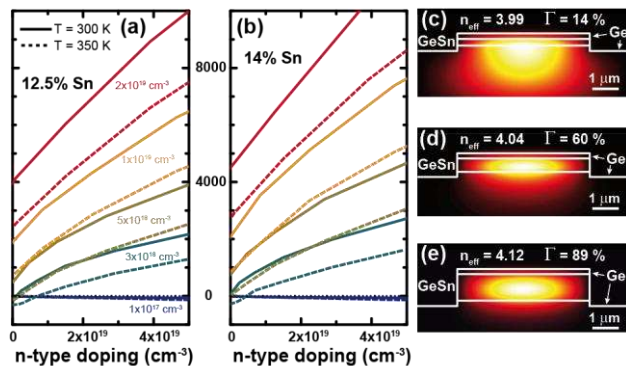
Fig. 9. Peak gain for in-plane polarization (TE mode) at T=300K (solid) and 350K (dashed) calculated for (a) 12.5 at.% and (b) 14 at.% GeSn samples for a range of doping and carrier injection densities. (c)-(e) Optical mode overlap with the active medium for GeSn thicknesses of 250 nm, 500 nm and 1μm, respectively.

The most important finding is that optical gain can be achieved in both samples even without any n-type doping. Optical gains as high as about 4200 cm^{-1} (12.5 at. % sample) and 4700 cm^{-1} (14 at. % sample) are predicted at 300 K for a carrier injection of 2×10^{19} cm^{-3} without any additional doping. They drop to ~2600 cm^{-1} and ~3000 cm^{-1}, respectively, for a (more likely) higher temperature of the active layer, T = 350 K. The Γ-L valley spacing in both samples amounts to ~60 meV, resulting from the opposing effects of alloy composition and compressive strain, as discussed before. As a consequence of the much larger density of states in the L-valleys, as mentioned above, only 8 % and 9 % of all electrons populate the Γ-valley, respectively. This leads to reasonably high gain values. The reason for the slightly higher gain in the 14 at.% sample is mainly the higher residual compressive strain, which makes the HH-LH splitting in it twice as large as in the 12.5 at.% sample, amplifying the fraction of 'useful' holes significantly. The optical gain can be further increased by n-type doping of the samples, as shown in Fig. 9(a) and (b). At highest carrier injections of 2×10^{19} cm^{-3}, an n-doping density of about 1.3×10^{19} cm^{-3} leads to a gain >6000 cm^{-1} at 300 K (>4000 cm^{-1} at 350 K) for the 12.5 at.% sample and a gain of 6800 cm^{-1} at 300 K (4800 cm^{-1} at 350 K) for the 14 at.% sample. Gain starts to saturate for even higher doping and/or injection levels. This is linked to the increasing role of FCA.

Thicker active medium layers not only increase the directness and therefore the lasing efficiency, but also improve the optical mode confinement in heterostructure lasers. This is illustrated in Figs. 9(c)-(e), where the calculated optical modes at a wavelength of 2.5 µm in a 5 µm wide optical waveguide are plotted for different layer thicknesses. Calculations [39] are based on a Ge-VS / GeSn / Ge cap

heterostructure which is suitable for electrically pumped lasing. In this design, the thick GeSn layer serves as the optical gain material, while the Ge cladding layers offer the appropriate band alignment for carrier confinement in the GeSn active area. The mode overlaps for 250 nm (b), 500 nm (c) and 1 µm (d) thick active GeSn layers are with such a design equal to 14 %, 60 % and 89 %, respectively.

4. Conclusions

In this work, we have described CVD growth of thick, single crystalline GeSn layers which are suitable for laser applications. The Sn content in the low-temperature grown films can be tuned between 5 at.% and 14 at.%, while maintaining a high crystalline quality for all layers with thicknesses up to 1 µm. AFM measurements did not show any sign of Sn segregation even for very thick layers. A cross-hatch is present at the surface of partially relaxed GeSn layers, however; its amplitude and the spatial wavelength of the undulations increased with the Sn content and the GeSn layer thickness. A plastic relaxation of the compressive strain that increases as the deposited thickness increases (all the way to 1 µm) was evidenced in 12.5 at.% Sn GeSn layers. TEM investigations showed that strain relaxation occurred through the formation of a regular array of edge misfit dislocations at the GeSn/Ge-VS interface and the emission of half-loops only in the VS. Such a strain relaxation process is very favorable for optoelectronic devices, as defects are not present in the bulk of the GeSn layers. Transmission/Reflection measurements evidenced the high optical quality of our GeSn layers and suggested a direct character of the bandgap, making these alloys useful for photon detection up to 3.5 µm. The photoluminescence spectra show strong light emission in the mid IR region. Tuning the directness of our layers (by increasing the Sn content or relaxing the residual compressive strain thanks to higher thicknesses), led to an even stronger PL response, demonstrating the potential of our GeSn layers as light-emitting devices. Optical gain calculations highlighted the potential of our GeSn layers for electrically pumped lasing (even without any doping).

In conclusion, these findings indicate a high potential of high Sn content, thick GeSn alloys for both active and passive optoelectronic devices (for instance electrically-pumped lasers) in the near- to mid-IR, with a huge variety of applications.

AUTHOR INFORMATION

Corresponding Author

* N. von den Driesch, n.von.den.driesch@fz-juelich.de ; Dan Buca, d.m.buca@fz-juelich.de .

Present Addresses

†T. Stoica is now with National Institute of Materials Physics, 077125, Magurele, Romania

References

(1)   Sanchez-Perez, J. R.; Boztug, C.; Chen, F.; Sudradjat, F. F.; Paskiewicz, D. M.; Jacobson, R.; Lagally, M. G.; Paiella, R. Proc. Natl. Acad. Sci. **2011**, 108 (47), 18893–18898.

(2)   Nam, D.; Sukhdeo, D.; Roy, A.; Balram, K.; Cheng, S.-L.; Huang, K. C.-Y.; Yuan, Z.; Brongersma, M.; Nishi, Y.; Miller, D.; Saraswat, K. Opt. Express **2011**, 19 (27), 25866.

(3)   Capellini, G.; Kozlowski, G.; Yamamoto, Y.; Lisker, M.; Wenger, C.; Niu, G.; Zaumseil, P.; Tillack, B.; Ghrib, A.; De Kersauson, M.; El Kurdi, M.; Boucaud, P.; Schroeder, T. J. Appl. Phys. **2013**, 113 (1), 013513.

(4)   Sukhdeo, D. S.; Nam, D.; Kang, J.-H.; Brongersma, M. L.; Saraswat, K. C. Photonics Res. **2014**, 2 (3), A8–A13.

(5)   Süess, M. J.; Geiger, R.; Minamisawa, R. a.; Schiefler, G.; Frigerio, J.; Chrastina, D.; Isella, G.; Spolenak, R.; Faist, J.; Sigg, H. Nat. Photonics **2013**, 7 (June), 466–472.

(6)   Liu, J.; Sun, X.; Pan, D.; Wang, X.; Kimerling, L. C.; Koch, T. L.; Michel, J. Opt. Express **2007**, 15 (18), 11272–11277.

(7)   Wirths, S.; Geiger, R.; von den Driesch, N.; Mussler, G.; Stoica, T.; Mantl, S.; Ikonic, Z.; Luysberg, M.; Chiussi, S.; Hartmann, J. M.; Sigg, H.; Faist, J.; Buca, D.; Grützmacher, D. Nat. Photonics **2015**, 9, 88–92.

(8)   Tonkikh, A. A.; Zakharov, N. D.; Suvorova, A. a.; Eisenschmidt, C.; Schilling, J.; Werner, P. Cryst. Growth Des. **2014**, 14 (4), 1617–1622.

(9)   Thurmond, C. D.; Trumbore, F. A.; Kowalchik, M. J. Chem. Phys. **1956**, 25 (4), 799.

(10)   Chen, R.; Huang, Y.-C.; Gupta, S.; Lin, A. C.; Sanchez, E.; Kim, Y.; Saraswat, K. C.; Kamins, T. I.; Harris, J. S. J. Cryst. Growth **2013**, 365, 29–34.

(11)   Gencarelli, F.; Vincent, B.; Demeulemeester, J.; Vantomme, A.; Moussa, A.; Franquet, A.; Kumar, A.; Bender, H.; Meersschaut, J.; Vandervorst, W.; Loo, R.; Caymax, M.; Temst, K.; Heyns, M. ECS J. Solid State Sci. Technol. **2013**, 2 (4), P134–P137.

(12)   Senaratne, C. L.; Gallagher, J. D.; Aoki, T.; Kouvetakis, J. Chem. Mater. **2014**, 26, 6033–6041.

(13)   Wirths, S.; Ikonic, Z.; Tiedemann, A. T.; Holländer, B.; Stoica, T.; Mussler, G.; Breuer, U.; Hartmann, J. M.; Benedetti, A.; Chiussi, S.; Grützmacher, D.; Mantl, S.; Buca, D. Appl. Phys. Lett. **2013**, 103 (19), 192110.

(14)   Oehme, M.; Kostecki, K.; Schmid, M.; Oliveira, F.; Kasper, E.; Schulze, J. Thin Solid Films **2014**, 557, 169–172.

(15)   Chen, R.; Lin, H.; Huo, Y.; Hitzman, C.; Kamins, T. I.; Harris, J. S. Appl. Phys. Lett. **2011**, 99 (18), 181125.

(16)   Homewood, K. P.; Lourenco, M. A. Nat. Photonics **2015**, 9 (2), 78–79.

(17)   Hartmann, J. M.; Abbadie, A.; Cherkashin, N.; Grampeix, H.; Clavelier, L. Semicond. Sci. Technol. **2009**, 24 (5), 055002.

(18)   Almond, M. J.; Doncaster, A. M.; Noble, P. N.; Walsh, R. J. Am. Chem. Soc. **1982**, 104, 4717–4718.

(19)   Takahashi, K.; Kunz, A.; Woiki, D.; Roth, P. J. Phys. Chem. A **2000**, 104 (22), 5246–5253.

(20)   Kasper, E.; Werner, J.; Oehme, M.; Escoubas, S.; Burle, N.; Schulze, J. Thin Solid Films **2012**, 520 (8), 3195–3200.

(21)   Bratland, K. A.; Foo, Y. L.; Spila, T.; Seo, H.-S.; Haasch, R. T.; Desjardins, P.; Greene, J. E. J. Appl. Phys. **2005**, 97 (4), 044904.

(22)   Wirths, S.; Buca, D.; Ikonic, Z.; Harrison, P.; Tiedemann, A. T.; Holländer, B.; Stoica, T.; Mussler, G.; Breuer, U.; Hartmann, J. M.; Grützmacher, D.; Mantl, S. Thin Solid Films **2014**, 557, 183–187.

(23) Fitzgerald, E. A.; Xie, Y. H.; Monroe, D.; Silverman, P. J.; Kuo, J. M.; Kortan, A. R.; Thiel, F. A.; Weir, B. E. J. Vac. Sci. Technol. B Microelectron. Nanom. Struct. **1992**, 10 (4), 1807.

(24) Bratland, K.; Foo, Y.; Soares, J.; Spila, T.; Desjardins, P.; Greene, J. Phys. Rev. B **2003**, 67 (12), 11–13.

(25) Bogumilowicz, Y.; Hartmann, J. M.; Laugier, F.; Rolland, G.; Billon, T.; Cherkashin, N.; Claverie, A. J. Cryst. Growth **2005**, 283 (3-4), 346–355.

(26) Trinkaus, H.; Buca, D.; Holländer, B.; Minamisawa, R. A.; Mantl, S.; Hartmann, J. M. J. Appl. Phys. **2010**, 107 (12), 1–8.

(27) LeGoues, F. K.; Meyerson, B. S.; Morar, J. F. Phys. Rev. Lett. **1991**, 66 (22), 2903–2906.

(28) Mosleh, A.; Ghetmiri, S. A.; Conley, B. R.; Hawkridge, M.; Benamara, M.; Nazzal, A.; Tolle, J.; Yu, S.-Q.; Naseem, H. a. J. Electron. Mater. **2014**, 43 (4), 938–946.

(29) Bahder, T. B. Phys. Rev. B **1990**, 41 (17), 11992–12001.

(30) Bahder, T. B. Phys. Rev. B **1992**, 46 (15), 9913.

(31) Tsai, C. Y.; Tsai, C. Y.; Chen, C. H.; Sung, T. L.; Wu, T. Y.; Shih, F. P. IEEE J. Quantum Electron. **1998**, 34 (3), 552–558.

(32) Virgilio, M.; Manganelli, C. L.; Grosso, G.; Pizzi, G.; Capellini, G. Phys. Rev. B **2013**, 87 (23), 235313.

(33) Trupke, T.; Green, M. a.; Würfel, P. J. Appl. Phys. **2003**, 93 (11), 9058–9061.

(34) Carroll, L.; Friedli, P.; Neuenschwander, S.; Sigg, H.; Cecchi, S.; Isa, F.; Chrastina, D.; Isella, G.; Fedoryshyn, Y.; Faist, J. Phys. Rev. Lett. **2012**, 109, 057402.

(35) Chang, G.-E.; Cheng, H. H. J. Phys. D. Appl. Phys. **2013**, 46 (6), 065103.

(36) Chang, G.; Member, S.; Chang, S.; Chuang, S. L. IEEE J. Quantum Electron. **2010**, 46 (12), 1813–1820.

(37) Lu Low, K.; Yang, Y.; Han, G.; Fan, W.; Yeo, Y.-C. J. Appl. Phys. **2012**, 112 (10), 103715.

(38) Ryu, M. Y.; Harris, T. R.; Yeo, Y. K.; Beeler, R. T.; Kouvetakis, J. Appl. Phys. Lett. **2013**, 102, 171908.

(39) Fallahkhair, A. B.; Li, K. S.; Murphy, T. E. J. Light. Technol. **2008**, 26 (11), 1423–1431.

For Use in Table of Contents/Abstract only: